Dynamics of stable viscous displacement in porous media

Eyvind Aker*, Knut Jørgen Måløy

Department of Physics, University of Oslo, N-0316 Oslo, Norway

Alex Hansen

Department of Physics, Norwegian University of Science and Technology, N-7491 Trondheim, Norway

(February 2, 2008)

We investigate the stabilization mechanisms of the invasion front in two-dimensional drainage displacement in porous media by using a network simulator. We focus on the process when the front stabilizes due to the viscous forces in the liquids. We find that the capillary pressure difference between two different points along the front varies almost linearly as function of height separation in the direction of the displacement. The numerical results support arguments that differ from those suggested earlier for viscous stabilization. Our arguments are based upon the observation that nonwetting fluid flows in loopless strands (paths) and we conclude that earlier suggested theories are not suitable to drainage when nonwetting strands dominate the displacement process. We also show that the arguments might influence the scaling behavior between the front width and the injection rate and compare some of our results to experimental work.

I. INTRODUCTION

Immiscible displacement of one fluid by another fluid in porous media has important applications in a wide range of different technologies. Most often mentioned is hydrology and oil recovery. From a theoretical point of view, the displacement process is very complex and hard to describe in detail. Especially, much attention has been paid to the rich variety of displacement structures that is observed. The displacement structures are found to depend strongly on the fluid properties like viscosity, interfacial tension, fluid flow rate, and wettability [1–4].

In drainage the primary process is the displacement of a wetting fluid by a nonwetting fluid in porous media. Consider a two-dimensional (2D) horizontal displacement of a less viscous fluid by a more viscous fluid. At high injection rates the front developing between the invading and defending fluid, is known to stabilize [3]. In contrast, at extremely low injection rate the invading fluid generates a growing cluster similar to the cluster formed by invasion percolation (IP) [5–8]. The displacement is now controlled solely by the capillary pressure, that is the pressure difference between the two fluids across a meniscus.

In this paper we address the question of how the invasion front stabilizes when no gravity forces are present (2D horizontal displacement). To do this, we have developed a network model that properly simulates the dynamics of the capillary pressures due to the menisci along the front as well as the viscous pressure buildup in the fluids. From the simulations we have calculated the capillary pressure difference $\Delta P_{c\parallel}$ between menisci along the front separated a distance Δh in the direction of the displacement. Also calculated, is the capillary pressure in the orthogonal direction $\Delta P_{c\perp}$, that is the capillary pressure between menisci at same height above the in-

let but separated a horizontal distance Δl (see Fig. 1). Simulations show that assuming a power law behavior $\Delta P_{c\parallel} \propto \Delta h^{\kappa}$, our best estimate of the exponent for a wide range of injection rates and different fluid viscosities is $\kappa = 1.0 \pm 0.1$. This is a surprising result because the viscous force field that stabilizes the front, is non homogeneous due to trapping of wetting fluid behind the front and to the fractal behavior of the front structure.

We also presents arguments being supported by the numerical evidence that $\kappa \simeq 1.0$. The arguments are based upon the observation that nonwetting fluid displaces wetting fluid through loopless strands (see Fig. 9). As a consequence, we find that existing theories [9–12] not considering this effect, are not compatible with drainage when nonwetting strands dominate the displacement process. We also conjecture that the result $\kappa \simeq 1.0$ may influence the scaling between the saturated front width w_s and the capillary number C_a. The capillary number is the ratio between viscous and capillary forces and in the following $C_a \equiv Q\mu_{nw}/\Sigma\gamma$. Here Q is the injection rate, Σ is the cross section of the inlet, and μ_{nw} is the viscosity of the nonwetting fluid.

The effect of gravity on the front when the fluids have different densities has been thoroughly discussed [13,9,14,15] and in slow drainage it is found that gravity may stabilize the front. Gravity causes a hydrostatic pressure gradient in the fluids and considering a heavy nonwetting fluid below displacing vertically upwards a light wetting fluid, this gradient will stabilize the front. The displacement process corresponds exactly to IP with a stabilizing gradient [9,14,16] and the saturated front width w_s, has been shown to scale like $w_s \propto B_o^{-\nu/(1+\nu)}$. Here ν is the correlation length exponent in percolation and B_o is the bond number indicating the ratio between gravity and capillary forces.

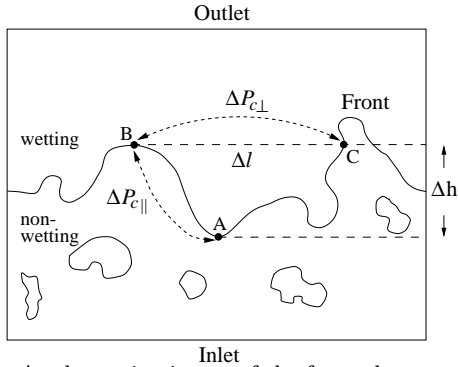A similar consensus concerning the stabilization mech-

FIG. 1. A schematic picture of the front that travels across the system from the inlet to the outlet. In the figure, $\Delta P_{c\parallel}$ is the capillary pressure difference between a meniscus at A and a meniscus at B separated a vertical distance Δh. In the orthogonal direction we calculate $\Delta P_{c\perp}$, that is the capillary pressure difference between a meniscus at B and a meniscus at C separated a horizontal distance Δl. ΔP_{nw} and ΔP_w denote the viscous pressure drop going from A to B in the nonwetting and wetting phase, respectively.

anisms when viscous forces replace gravity forces has not yet been reached. In the literature the displacement has been related to IP [9,11,12], however, the scenario is more complicated than in the gravity case. Gravity is a uniform force acting on the whole system, while the viscous force is local and fluctuates due to permeability variations and fluid trapping in the porous medium. One standard approach is to separate the displacement structure into two parts. One consisting of the frontal region, and the other consisting of the static structure behind. The frontal region of extent w_s, is assumed to behave as the spanning cluster in percolation. Consequently, it is assigned the permeability $k \propto w_s^{-t/\nu}$, where t is the conductivity exponent in percolation. By applying Darcy's law and assuming that the stabilized front reaches a traveling-wave state according to Buckley-Leverett displacement [17], the scaling of the front width is found to behave as $w_s \propto C_a{}^{-\alpha}$. In the literature there exists two slightly different expression for α. In 3D Wilkinson [9] found $\alpha = \nu/(1 + t - \beta + \nu)$ where trapping of wetting fluid is assumed to be less important. Here β is the order parameter exponent in percolation. Later, Blunt et al. [11] suggested in 3D that $\alpha = \nu/(1 + t + \nu)$ which is identical to the result of Lenormand [10] discussing limits of fractal patterns between capillary fingering and stable displacement in 2D porous media. In Appendix A we present a simple method giving $\alpha = \nu/(1 + t - \beta + \nu)$ by applying percolation concepts on the frontal region when not considering that nonwetting fluid flows in strands.

Recently, Xu et al. [12] used Wilkinson's arguments and deduced a scaling relation for the viscous pressure drops in the frontal region. They proposed that the non-wetting pressure drop ΔP_{nw} in the front (see Fig. 1) should scale as $\Delta P_{nw} \propto \Delta h^{t/\nu + d_E - 1 - \beta/\nu}$ over a distance

Δh in the direction of the displacement. Here, d_E is the Euclidean dimension of the space in which the front is embedded (in our case $d_E = 2$) and Δh is assumed to be sufficiently large for scaling to be acceptable and less than w_s. They also argued that the pressure drop in the wetting phase ΔP_w, must be linearly dependent on Δh, since the displaced phase is compact. In [11] Blunt et al. also suggested a scaling relation for ΔP_{nw}, however, in 3D they found $\Delta P_{nw} \propto \Delta h^{t/\nu + 1}$. This deviates from the result of Xu et al. when $d_E = 3$.

The paper is organized as follows. In Sec. II we describe the network model used in the simulations. Sec. III contains the simulation results of $\Delta P_{c\parallel}$ and $\Delta P_{c\perp}$, supporting the arguments we present in Sec. IV. In Sec. V we compare our findings to some experimental data and the conclusions are drawn in Sec. VI. At the end we have put Appendix A where we deduce the scaling relation between w_s and C_a using the ideas in [9] when not considering the effect of nonwetting fluid flowing in strands.

II. NETWORK MODEL

The network model has been presented elsewhere [18,19] and therefore only its main features will be given here.

In the simulations we have constructed the porous medium in two different ways. In the first way the porous medium is represented by a square lattice of tubes oriented at 45°. The tubes are cylindrical with length d. Each tube between the ith and the jth node in the lattice is assigned an average radius r_{ij} which is chosen at random in the interval $[\lambda_1 d, \lambda_2 d]$, where $0 \leq \lambda_1 < \lambda_2 \leq 1$. The randomness of the radii represents the disorder in the system. In the following this system will be referred to as the random radii lattice.

In the second way the porous medium is constructed upon a square lattice inclined 45° where the distance between each intersection in the lattice is of unit length. Around each intersection we draw a circle of radius λ. To avoid overlapping circles the given λ must be in the interval $0 \leq \lambda < 1/2$. A node is placed at random inside each of the circles and the nodes inside the nearest neighbor circles are connected by cylindrical tubes. Thus, as for the random radii lattice, four tubes meet at each node. We let d_{ij} denote the length of the tube between the ith and jth node, and the corresponding radius r_{ij} is defined as $r_{ij} = d_{ij}/2\alpha$. Here α is the aspect ratio between the tube length and the radius. In the simulations $\alpha = 1.25$, hence, the tubes are 25% longer than they are wide. In this lattice the position of the nodes represent the disorder in the system, and therefore we will refer to it as the random node lattice.

While every pair of nearest neighbor nodes are separated an equal distance in the random radii lattice, the distance between two nearest neighbor nodes vary in

the random node lattice. Especially, the shortest length scale, that is the minimum distance between two neighboring nodes, is less in the random node lattice. Consequently, we are able to generate more narrow fronts at higher injection rates in the random node lattice, than what is possible with the random radii lattice. Therefore the random node lattice is preferred at high injection rates where a flat front is generated.

In both lattices the tubes represent the volume of both pores and throats, and there is no volume assigned to the nodes. The liquids flow from the bottom to the top of the lattice, and we implement periodic boundary conditions in the horizontal direction. The pressure difference between the bottom row and the top row defines the pressure across the lattice. Initially, the system is filled with a wetting fluid with viscosity μ_w. The injected fluid is nonwetting and has viscosity $\mu_{nw} \geq \mu_w$. The viscosity ratio M, is defined as $M \equiv \mu_{nw}/\mu_w$.

The capillary pressure p_c between the nonwetting and wetting fluid in a tube is given by Young-Laplace law

$$p_c = \gamma \left(\frac{1}{R_1} + \frac{1}{R_2} \right), \tag{1}$$

where R_1 and R_2 are the principal radii of curvature of the interface (a meniscus) and γ is the interfacial tension. In a cylindrical tube of radius r where $R_1 = R_2$, Eq. (1) reduces to $p_c = (2\gamma/r)\cos\theta$. Here θ denotes the wetting angle between the nonwetting and wetting phases, and in drainage θ is in the interval $(0, \pi/2)$.

In the network model we treat the tubes as if they were hourglass shaped with effective radii following a smooth function. Hence, we let the capillary pressure become a function of the meniscus position in the tube and assume the Young-Laplace law (1) takes the form

$$p_c = \frac{2\gamma}{r} \left[1 - \cos(2\pi\tfrac{x}{d}) \right]. \tag{2}$$

Here $0 \leq x \leq d$ is the position of the meniscus in the tube where d is the tube length. We assume perfect wetting, i.e. $\theta = 0$.

By letting p_c vary according to (2), we include the effect of burst dynamics into the model [18]. This is particularly seen at low injection rates where the invasion of nonwetting fluid takes place in bursts accompanied by sudden negative jumps in the pressure (Haines jumps) [20–22]. The detailed modelling of the capillary pressure costs computation time. However, it is necessary in order to properly simulate the pressure behavior along the front.

The volume flux q_{ij} through a tube from the ith to the jth node is found from the Washburn equation for capillary flow [23]

$$q_{ij} = -\frac{\sigma_{ij}k_{ij}}{\mu_{ij}} \frac{1}{d_{ij}} (\Delta p_{ij} - p_{c,ij}). \tag{3}$$

Here k_{ij} is the permeability of the tube $(r_{ij}^2/8)$ and σ_{ij} is the cross section (πr_{ij}^2) of the tube. μ_{ij} is the effective

viscosity given by the sum of the volume fractions of each fluid inside the tube multiplied by their respective viscosities. The pressure drop across the tube is $\Delta p_{ij} = p_j - p_i$, where p_i and p_j is the nodal pressures at node i and j respectively. The capillary pressure $p_{c,ij}$ is the sum of the capillary pressures of the menisci (given by Eq. (2)) inside the tube. A tube partially filled with both liquids, is allowed to contain either one or two menisci. For a tube without menisci $p_{c,ij} = 0$, and Eq. (3) reduces to that describing Hagen-Poiseuille flow with $\mu_{ij} = \mu_1$ or μ_2.

We assume conservation of volume flux at each node giving

$$\sum_j q_{ij} = 0. \tag{4}$$

The summation on j runs over the nearest neighbor nodes to the ith node while i runs over all nodes that do not belong to the top or bottom rows, that is, the internal nodes.

Eqs. (3) and (4) constitute a set of linear equations which are to be solved for the nodal pressures p_i, with the constraint that the pressures at the nodes belonging to the upper and lower rows are kept fixed. The set of equations is solved by using the Conjugate Gradient method [24].

During every simulation we held the injection rate Q fixed and calculate a time dependent pressure ΔP across the system. See Refs. [18,19] for details on how ΔP and the corresponding p_i's are found.

Having found the p_i's we calculate the volume fluxes, q_{ij}, through every tube in the network, using Eq. (3). According to the q_{ij}'s we define a time step Δt, such every meniscus is allowed to travel at most a maximum step length $\Delta x_{\max}$, during that time step. The menisci are then moved a distance $(q_{ij}/\sigma_{ij})\Delta t$ and the pressure ΔP and the time lapse are recorded, before the p_i's are solved for the new fluid configuration. Menisci that are moved out of a tube during a time step are spread into neighbor tubes. For details about how the menisci is moved into neighbor tubes see Refs. [18,19].

Numerical simulations show that $\Delta x_{\max}$ must be of order 0.1 to calculate the variation in the capillary pressure when a meniscus travel through a tube. In all simulations presented here $\Delta x_{\max} = 0.1$, resulting in at least ten time steps to invade one tube with nonwetting fluid. This causes the computation time to increase dramatically and one displacement simulation on lattices of sizes presented in this paper takes typically between 3–15 hours on a 400 MHz Pentium II processor.

III. SIMULATIONS

We have run drainage simulations at different injection rates and fluid viscosities to study the capillary pressure

variations along the invasion front. Due to the huge computational effort that is necessary, the simulations have been limited to lattices of size 25×35 and 40×60 nodes (Sec. III A). We have also run some simulations where the lattice initially was filled with nonwetting and wetting fluid according to patterns which were generated by an IP algorithm (Sec. III C). In this way, we were able to study the capillary pressure along invasion fronts on lattices of 200×300 nodes.

In every simulation, $\Delta P_{c\parallel}$, $\Delta P_{c\perp}$, and the front width between the invading and the defending fluid, was recorded. The front was detected by running a Hoshen-Kopelman algorithm [25] on the lattice and recognized as the set of tubes that contain a front meniscus between the nonwetting and wetting phase, that is the front tubes. The front width w is defined as the standard deviation of the vertical distances between front tubes and the average position of the front. Let h_i denote the vertical distances of the front tubes above the inlet, where $i = 1, ..., n_f$ and n_f is the total number of front tubes. Then at a particular time, we calculate $w = [(1/n_f) \sum_i (h_i - h)^2]^{1/2}$, where h is the average of the h_i's.

$\Delta P_{c\parallel}$ and $\Delta P_{c\perp}$ is calculated as follows. Consider two front menisci denoted by m and n with height h_m and h_l above the inlet (bottom row) at a distance l_m and l_n from the left boundary of the lattice. Assume that $h_m > h_n$, then we calculate the difference $\Delta P_c^{mn}(\Delta h, \Delta l) = p_c^n - p_c^m$ where $\Delta h = h_m - h_n$ and $\Delta l = |l_m - l_n|$. If instead $h_n > h_m$, we compute $\Delta P_c^{nm}(\Delta h, \Delta l) = p_c^m - p_c^n$ where $\Delta h = h_n - h_m$. We only consider the front tubes containing one meniscus and where the nonwetting fluid invades the tube from below. Note also, that we always take the capillary pressure of the meniscus closest to the inlet minus the capillary pressure of the meniscus closest to the outlet. From above, we define $\Delta P_{c\parallel}$ as function of Δh as the average of ΔP_c^{mn} over all pairs mn separated a distance Δh but different Δl, i.e $\Delta P_{c\parallel} = \langle \Delta P_c^{mn}(\Delta h = \text{const.}, \Delta l) \rangle$.

The capillary pressure difference in the orthogonal direction, $\Delta P_{c\perp}$, (parallel to the inlet) as function of Δl is defined as the average of $|\Delta P_c^{mn}|$ over all pairs mn with equal height ($\Delta h = 0$) above the inlet when Δl is held constant. Thus, in the above notation $\Delta P_{c\perp} = \langle |\Delta P_c^{mn}(0, \Delta l = \text{const.})| \rangle$.

The simulations were performed with parameters as close as possible to experiments performed in [26]. In the random radii lattice we set the length d, of all tubes equal to 1 mm and the radii r of the tubes were randomly chosen in the interval $0.05d \le r \le d$. In the lattices with random nodes we chose the positions of the nodes such that the length of the tubes were inside the interval $0.2 \le d \le 1.8$ mm. This gave us the radii of the tubes, defined by $r = d/2\alpha$, where $\alpha = 1.25$. For both types of lattices the interfacial tension was set to $\gamma = 30$ dyn/cm, and the fluid viscosities were 0.10 P, 0.50 P or 10 P.

TABLE I. Simulations performed on the random radii lattice of size 25×35 nodes and $M = 100$ ($\mu_{nw} = 10$ P, $\mu_w = 0.10$ P). The table contains the number of runs at each Q and C_a and the calculated w_s.

Runs	Q (cm^3/min)	C_a	w_s
30	0.050	3.7×10^{-4}	5.5 ± 0.5
30	0.10	7.3×10^{-4}	4.3 ± 0.4
30	0.20	1.5×10^{-3}	3.7 ± 0.4
30	0.50	3.7×10^{-3}	3.0 ± 0.3
30	0.80	5.8×10^{-3}	2.5 ± 0.3
30	1.5	1.1×10^{-2}	2.4 ± 0.2

TABLE II. Simulations performed on the random node lattice of size 25×35 nodes and $M = 100$ ($\mu_{nw} = 10$ P, $\mu_w = 0.10$ P). The table contains the number of runs at each Q and C_a, and the calculated w_s.

Runs	Q (cm^3/min)	C_a	w_s
10	0.010	1.0×10^{-4}	4.3 ± 0.6
20	0.030	3.1×10^{-4}	2.9 ± 0.3
20	0.050	5.2×10^{-4}	2.5 ± 0.2
20	0.10	1.0×10^{-3}	2.1 ± 0.2
20	0.30	3.1×10^{-3}	1.4 ± 0.1
15	0.50	5.2×10^{-3}	1.2 ± 0.1
15	1.0	1.0×10^{-2}	0.9 ± 0.1
10	2.0	2.1×10^{-2}	0.8 ± 0.1
10	4.0	4.2×10^{-2}	0.8 ± 0.1

A. Capillary pressure behavior

We have performed two series of simulations with viscosity ratio $M = 100$ and one series of viscosity matched fluids, $M = 1$. In all series the capillary number C_a, was systematically varied by changing the injection rate Q. Tables I, II, and III list Q, C_a and the type of lattice (random radii or random nodes) used in the different series. Also shown are the calculated front width w_s, and the number of different runs we did at each Q to obtain reliable average quantities.

TABLE III. Simulations performed on the random node lattice of size 40×60 nodes and $M = 1$ ($\mu_{nw} = \mu_w = 0.50$ P). The table contains the number of runs at each Q and C_a and the calculated w_s.

Runs	Q (cm^3/min)	C_a	w_s
10	0.050	1.6×10^{-5}	7.5 ± 1.5
10	0.10	3.2×10^{-5}	6.9 ± 1.2
15	0.30	9.7×10^{-5}	5.2 ± 0.5
15	0.60	1.9×10^{-4}	4.4 ± 0.5
20	1.2	3.9×10^{-4}	3.8 ± 0.5
20	2.4	7.8×10^{-4}	3.0 ± 0.2
20	4.8	1.6×10^{-3}	2.4 ± 0.2

4

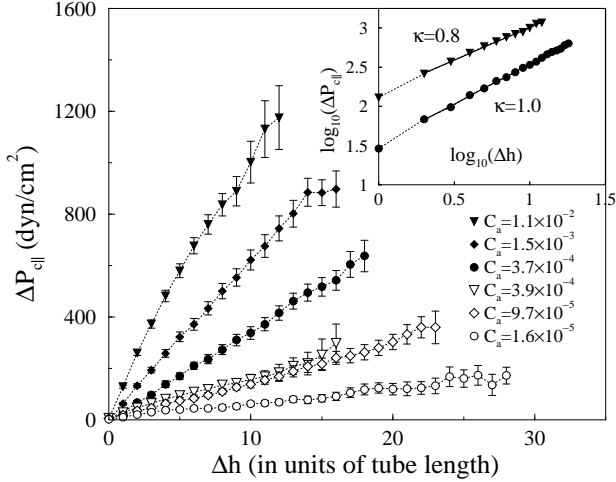FIG. 2. $\Delta P_{c\parallel}$ as function of Δh for some C_a with $M = 100$ (Table I) and $M = 1$ (Table III). $\Delta P_{c\parallel}$ is the average of the different runs performed at each C_a, and the error bars denote the standard error of the mean. *Inset:* $\log_{10}(\Delta P_{c\parallel})$ as function of $\log_{10}(\Delta h)$ for $C_a = 1.1 \times 10^{-2}$ and $C_a = 3.7 \times 10^{-4}$ with $M = 100$. The solid lines were fitted to the curves and their slopes are given by κ.

Fig. 2 shows the calculated capillary pressure difference $\Delta P_{c\parallel}$, in the direction of the displacement as function of height separation Δh. We have plotted the result for some of the simulations performed on the random radii lattice of 25×35 nodes with $M = 100$ (filled symbols) and for some of the random node lattice of 40×60 nodes with $M = 1$ (open symbols). In the inset of Fig. 2 the results for highest and lowest C_a with $M = 100$, are plotted in a logarithmic plot and fitted to straight lines. Assuming a power law behavior, we find that at $C_a = 3.7 \times 10^{-4}$ and $M = 100$, $\Delta P_{c\parallel} \propto \Delta h^{\kappa}$ and $\kappa = 1.0$. The exponent κ seems to decrease systematically with increasing injection rate, and at $C_a = 1.1 \times 10^{-2}$ and $M = 100$ our best estimate is $\kappa = 0.8$. Similar results was found from the simulations performed with viscosity matched fluids ($M = 1$). The data points corresponding to $\Delta h \leq 1$ tube length, is omitted in the calculations of the exponent in Fig. 2. At short distances we expect uncertainties in the result because of the finite length of the tubes in the lattice.

In Fig. 2 we observe that $\Delta P_{c\parallel}$ increases more rapidly as function of Δh at high injection rates compared to the results at low injection rates. In the plot the effect is most significant when $M = 100$. At extremely low injection rate we expect $\Delta P_{c\parallel}$ in Fig. 2 to approach zero and become independent of Δh. In this limit the capillary pressure of the menisci along the front are almost equal (capillary equilibrium). As seen from Fig. 2, we have not performed simulations with that low injection rate. Instead the lowest C_a for $M = 100$ and $M = 1$, corresponds to the injection rate where no clear stabilization of the
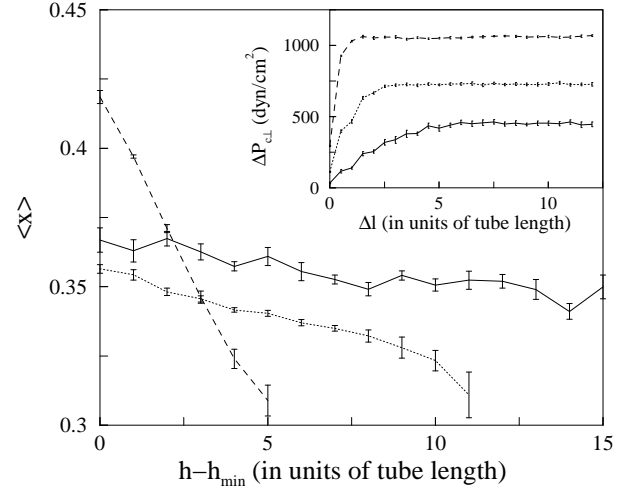

FIG. 3. The average position $\langle x \rangle$, of the front menisci inside the tubes as function of the menisci's height h relative to the of bottom height of the front $h_{\min}$. The plot shows result from simulations in Table II at $C_a = 1.0 \times 10^{-4}$ (solid line), 1.0×10^{-3} (dotted line), and 1.0×10^{-2} (dashed line). *Inset:* The corresponding $\Delta P_{c\perp}$ as function of Δl. The lattice size was 25×35, giving a maximum horizontal distance $\Delta l = 12.5$ due to the periodic boundary conditions in the horizontal direction. The error bars denote the standard error in the mean.

front was found due to the finite size of the system.

At higher injection rates the viscous gradient stabilizes the front. The gradient results the capillary pressure of the menisci closest to the inlet to exceed the capillary pressure of the menisci further down the stream. This is indicated in Fig. 3, showing the average position $\langle x \rangle$ of the front menisci inside the tubes as function of their vertical height h, relative to the bottom height of the front $h_{\min}$. $\langle x \rangle$ is plotted for high, intermediate, and low C_a for the simulations listed in Table II. From the figure we observe that at high $C_a = 1.0 \times 10^{-2}$ (dashed line), the menisci near $h_{\min}$ is placed closer to the middle of the tube compared to the menisci ahead. Consequently, the capillary pressure of the menisci near $h_{\min}$ will more likely be larger than the capillary pressure of the menisci away from $h_{\min}$ and therefore tubes near $h_{\min}$ will more easily be invaded. This will eventually stabilize the front. Remember that the tubes are hourglass shaped and most narrow at $x = 0.5$ (see Eq. (2)). At low injection rate, $C_a = 1.0 \times 10^{-4}$ (solid line), we approach the regime of capillary equilibrium giving almost no difference in $\langle x \rangle$ as function of $h - h_{\min}$.

For the three C_a's in Fig. 3 we have also calculated the capillary pressure difference in the orthogonal direction, $\Delta P_{c\perp}$, as function of horizontal distance, Δl. The result is shown in the inset of Fig. 3. Here we interpret $\Delta P_{c\perp}$ as the horizontal correlations in the capillary pressure between menisci at same height. Recall that $\Delta P_{c\perp}$
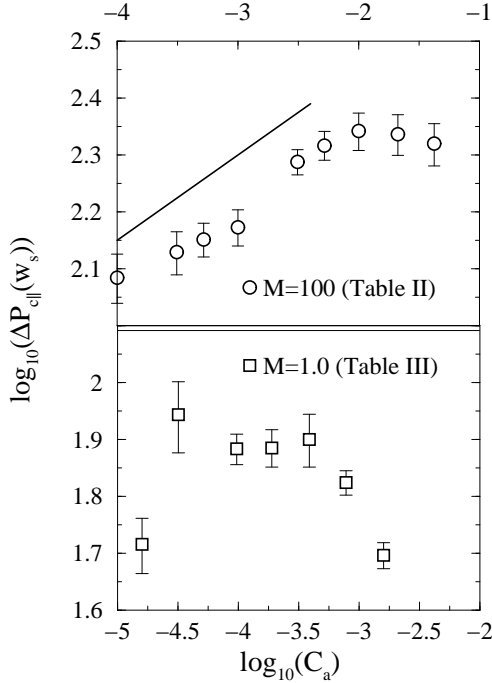
5

FIG. 4. $\log_{10}(\Delta P_{c\parallel}(w_s))$ as function of $\log_{10}(C_a)$ for the simulations performed on the random node lattice with $M = 100$ (top) and $M = 1$ (bottom). The slope of the solid line in the upper figure is 0.15. The error bars denote the standard error in the mean.

contains terms like $|p_c^m - p_c^n| = \sqrt{(p_c^m - p_c^n)^2}$, where p_c^m and p_c^n denote the capillary pressure of two front menisci m and n, respectively. From the inset of Fig. 3 we see that at low $C_a = 1.0 \times 10^{-4}$ (solid line) the capillary pressure of two menisci at same height and a distance $\Delta l \lesssim 7$ apart, are correlated to each other because $\Delta P_{c\perp}$ as not yet reached the constant plateau ($\Delta l > 7$) where the capillary pressures becomes uncorrelated. At short distances $\Delta P_{c\perp}$ approaches zero, indicating that neighboring menisci have equal capillary pressures. At high $C_a = 1.0 \times 10^{-2}$ (dashed line), we observe that the correlations are very short. Already for $\Delta l > 1$, $\Delta P_{c\perp}$ reaches the plateau and the capillary pressures of the menisci do no longer interfere. Thus, if we consider a narrow and a wide tube at same height, the viscous forces are strong enough to push the nonwetting fluid through both the narrow and the wide tube simultaneously. As a result nonwetting fluid will invade simultaneously everywhere along the front. Similar behavior is observed in the other simulations listed in Tables I and III at high C_a

B. Effect of viscosity ratio on the capillary pressure

Fig. 4 shows a log-log plot of $\Delta P_{c\parallel}$ taken at $\Delta h = w_s$, as function of C_a for the simulations performed on the random node lattice with $M = 100$ (Table II) and

$M = 1$ (Table III). In the following $\Delta P_{c\parallel}$ at w_s is denoted as $\Delta P_{c\parallel}(w_s)$. If we ignore the effect of nonwetting strands and use the result presented in Appendix A on our problem, we have that $\Delta P_{c\parallel}(w_s) \propto C_a w_s{}^\kappa$ by setting $\Delta h = w_s$ in Eq. (A1). Here $w_s \propto C_a{}^{-\alpha}$ where $\alpha = \nu/(1 + t - \beta + \nu)$ and $\kappa = t/\nu + 1 - \beta/\nu$ according to Appendix A. By combining the two power laws we obtain $\Delta P_{c\parallel}(w_s) \propto C_a{}^{1/(1+t-\beta+\nu)}$ giving in 2D, $\Delta P_{c\parallel}(w_s) \propto C_a{}^{0.29}$.

If we assume a power law behavior between $\Delta P_{c\parallel}(w_s)$ and C_a, our best result for the exponent is 0.15 ± 0.05 when $M = 100$ in Fig. 4. Note that there seems to be an upper cut off at $C_a \gtrsim 1.0 \times 10^{-2}$ where $\Delta P_{c\parallel}(w_s)$ stops growing. At $C_a \gtrsim 1.0 \times 10^{-2}$ the front is typically flat and we approach the minimum width due to the finite length of the tubes (see Table II). In this limit we expect a cross over to another type of behavior.

If it is difficult to confirm any power law when $M = 100$, the result of $M = 1$ in Fig. 4 does not show any scaling behavior. Already for $C_a \gtrsim 1 \times 10^{-4}$, $\Delta P_{c\parallel}(w_s)$ reaches a plateau or even decreases. To explain the different behavior of $\Delta P_{c\parallel}(w_s)$ when $M = 1$ and 100, we first look at the strength of the capillary pressure drop across the front and second we compare that to the magnitude of $\Delta P_{c\perp}$ as function of C_a.

To study the capillary pressure drop we have calculated the average capillary pressure $\langle P_c \rangle$ in the frontal region as function of the relative height from the bottom of the front, $(h - h_{\min})/w_s$. The height is normalized by dividing with the saturated front width w_s. In the simulations $\langle P_c \rangle$ was computed by taking the average of the capillary pressures of the front menisci at same height, h, above the inlet. Fig. 5 shows the result for two simulations with almost equal C_a but different M. One with $M = 1$ and $C_a = 1.6 \times 10^{-3}$ (Table III) and the other with $M = 100$ and $C_a = 1.0 \times 10^{-3}$ (Table II). If we consider the middle part of the front between the two vertical dashed lines in Fig. 5, we observe that the capillary pressure drop, $-w_s d\langle P_c \rangle/dh$, over a length w_s in the front, is higher for $M = 100$ than for $M = 1$, even though the capillary numbers are almost equal. In both simulations a typical narrow front with a compact displacement structure developed. On average, $-w_s d\langle P_c \rangle/dh$ must equal the difference between the pressure drops taken in the nonwetting and wetting part of the front over a length w_s (see Fig. 1). When the nonwetting and wetting fluid have equal viscosities the pressure drops in the nonwetting and wetting part of the front is about the same, explaining the smaller capillary pressure drop when $M = 1$ than when $M = 100$ in Fig. 5.

Let us now study the behavior of $\Delta P_{c\perp}$. Simulations show that $\Delta P_{c\perp}$ as function of Δl does not change much when comparing simulations performed at equal C_a with $M = 1$ and $M = 100$. Especially, the constant plateau where the capillary pressures are uncorrelated (see inset of Fig. 3), has the same value. This is illustrated in Fig. 6 where we have plotted the plateau of $\Delta P_{c\perp}$ versus
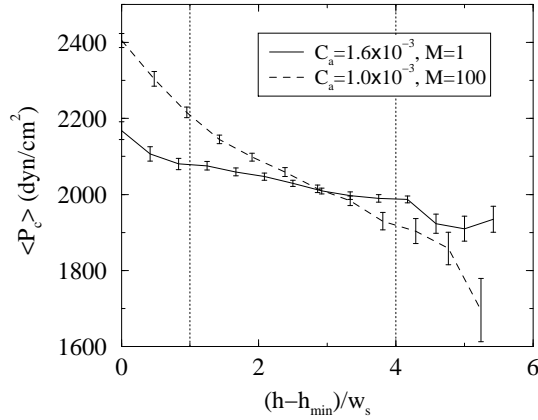
FIG. 5. $\langle P_c \rangle$ in the frontal region as function of the relative height from the bottom of the front. The height distance is normalized by dividing with the saturated front width w_s. The vertical dashed lines indicate the region where $\langle P_c \rangle$ is approximately linear. The error bars denote the standard error of the mean.
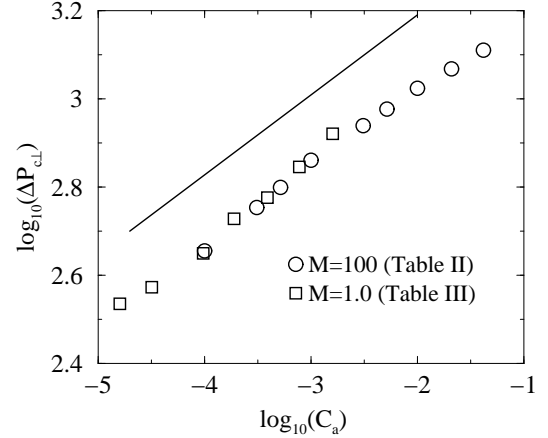

FIG. 6. The logarithm of the plateau of $\Delta P_{c\perp}$ versus the logarithm of C_a for $M = 100$ (circles) and $M = 1$ (boxes) corresponding to simulations listed in Table II and Table III, respectively. The slope of the solid line is 0.2. See also the inset of Fig. 3.

C_a in a logarithmic plot for simulations with $M = 100$ (Table II) and $M = 1$ (Table III). From the figure we observe that the plateau does not depend on M. As a side mark, we notice that there seems to be a power law between the plateau of $\Delta P_{c\perp}$ and C_a, which we indicate by the straight line in Fig. 6. The slope of the line is 0.2.

From the above discussion we draw the following conclusion. Consider two parallel and horizontal lines intersecting the front and let the lines be separated a vertical distance w_s. When $M = 1$ we have found that the capillary pressure drop between the lines is small due to the equal fluid viscosities (Fig. 5). However, the magnitude (plateau) of $\Delta P_{c\perp}$, is found to be the same as when $M = 100$ (Fig. 6). Thus, when $M = 1$ the relative small capillary pressure drop is annihilated by the magnitude of the capillary variations in the horizontal direction, $\Delta P_{c\perp}$. This destroys a possible power law behavior of $\Delta P_{c\parallel}(w_s)$ when $M = 1$ in Fig. 4. When $M = 100$, the capillary variations are too small to annihilate the larger capillary pressure drop there, giving the increasing function $\Delta P_{c\parallel}(w_s)$. If we divide the capillary pressure drop, calculated in Fig. 5, with the plateau of $\Delta P_{c\perp}$ in Fig. 6, we find that the ratio is a factor three lower for $M = 1$ than for $M = 100$ at $C_a \simeq 1.0 \times 10^{-3}$.

C. Capillary pressure on IP patterns

We have studied the capillary pressure along the front of patterns generated by an IP algorithm with a stabilizing gradient. The patterns were loaded into our network model, and the simulations were started from that point. Using this method, we were able to perform displacement simulations in a short period of time on patterns generated on lattices of 200×300 nodes. The result of these

simulations are based on the assumption that the generated patterns are statistically equal to the structures that would have been obtained in a corresponding complete displacement simulation.

The IP algorithm was performed on the bonds in a square lattice with the bonds oriented at $45°$. Hence, the bonds correspond to the tubes in our network model and an occupied bond refers to a tube filled with nonwetting fluid. Each bond were assign a random number f_{ij} in the interval $[0, 1]$ where ij denote the bond between the ith and the jth node in the lattice. A stabilizing gradient g was applied on the lattice giving an occupation threshold t_{ij} of every bond like, $t_{ij} = f_{ij} + g h_{ij}$ [9,14]. Here h_{ij} denotes the height of bond ij above the bottom row. The occupation of bonds started at the bottom row, and new bonds were occupied until the invasion front reached the top row. There was periodic boundary conditions in the horizontal direction. The next bond to be occupied was defined as the bond with the lowest threshold value from the set of empty bonds along the invasion front. The invasion front was found by running a Hoshen-Kopelman algorithm on the lattice.

We generated four IP patterns with $g = 0.05$ and different sets of random numbers f_{ij}. When the invasion front became well developed with trapped (wetting) clusters of all sizes between the size of the bonds and the front width, the structures were loaded into our network model. Fig. 7 shows one of the generated IP patterns.

The loading was performed by filling the tubes in the network model with nonwetting and wetting fluid according to occupied and empty bonds in the IP lattice. Furthermore, the radii r_{ij} of the tubes were mapped to the random numbers f_{ij} of the bonds like, $r_{ij} = [\lambda_1 + (\lambda_2 - \lambda_1)(1 - f_{ij})]d$. Thus, $r_{ij} \in [\lambda_1 d, \lambda_2 d]$ where, we set the tube length $d = 1$ mm, $\lambda_1 = 0.05$, and $\lambda_2 = 1.0$.
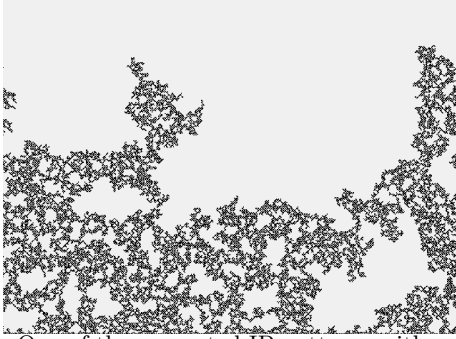
7

FIG. 7. One of the generated IP patterns with $g = 0.05$ on a lattice of 200×300 nodes. The pattern was loaded into our network model.

Above, r_{ij} is mapped to $1 - f_{ij}$ because in the IP algorithm the next bond to be invaded is the one with the lowest threshold value, opposite to the network model, where the widest tubes will be invaded first. Note also, that in the network model the invasion of nonwetting fluid is controlled by the threshold capillary pressures p_t of the tubes. According to Eq. (2) $p_t = 4\gamma/r$ in the middle of the tubes where $x = d/2$. In the IP model the distribution of f_{ij} is flat. Thus, when r_{ij} is mapped to f_{ij} as described above, we obtain a $1/p_t{}^2$ distribution of capillary pressure thresholds. However, since there is a one to one correspondence in the mapping between f_{ij} and p_t, we can assume that the IP patterns are statistically equal to similar structures that would have been generated in a full displacement simulation. The assumption provides that the displacement simulation is performed with an appropriate injection rate Q, according to g that was used to generate the IP patterns.

After the IP patterns were successfully loaded into the network model, we started the simulations and ran the displacement a limited number of time steps while $\Delta P_{c\parallel}$ was recorded. The number of time steps were chosen such that the front menisci got sufficient time to adjust according to the viscous pressure set up by the injection rate. For all four structures we chose $M = 100$ and $Q = 0.1$ ml/min, giving $C_a = 9.5 \times 10^{-5}$. This C_a might be too high compared to the front widths we obtained at low C_a from simulations listed in Tables I and II. The reason why we choose a high C_a is to minimize computation time. Simulations show that fewer time steps and hence, less CPU time are required to adjust the front menisci when a high injection rate is applied instead of a low one. Moreover, the simulations also show that as long as the number of time steps are chosen sufficiently large to allow the front menisci to adjust, the exponent κ in $\Delta P_{c\parallel} \propto \Delta h^\kappa$, is not sensitive on the injection rate. In the present simulations the number of time steps was 400.

The result of the simulations is shown in Fig. 8 where we have plotted $\log_{10}(\Delta P_{c\parallel})$ versus $\log_{10}(\Delta h)$. As for the previous results, we find $\kappa = 1.0 \pm 0.1$. The slope
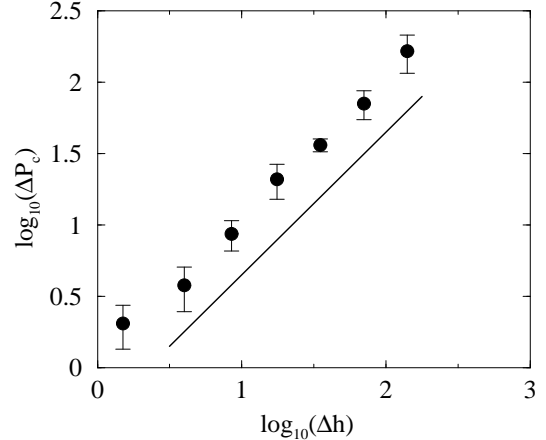

FIG. 8. $\log_{10}(\Delta P_{c\parallel})$ as function of $\log_{10}(\Delta h)$ for simulations initiated on IP patterns on lattices of 200×300 nodes. $C_a = 9.5 \times 10^{-5}$ and $M = 100$. The result is averaged over four different runs and the error bars denote the standard error in the mean. The slope of the straight solid line is 1.0.

of the straight line in Fig. 8 is 1.0. We have also done displacement simulations on one of the IP patterns at $C_a = 2 \times 10^{-6}$ with $M = 1$ and $M = 100$. These simulations were run in 1600 time steps and the result of those is consistent with Fig. 8.

IV. EFFECT OF LOOPLESS STRANDS

In [12] it was argued that $\Delta P_{c\parallel} = \Delta P_{nw} - \Delta P_w$ (see Fig. 1). At low injection rates or when the nonwetting phase is much more viscous than the wetting phase, $\Delta P_w \ll \Delta P_{nw}$, giving $\Delta P_{c\parallel} \sim \Delta P_{nw}$. Thus, if the result of Xu et al. [12] should be valid for our problem, we would expect to find $\Delta P_{c\parallel} \propto \Delta h^\kappa$ where $\kappa = t/\nu + d_E - 1 - \beta/\nu$. Inserting values of the exponents in 2D ($t = 1.3$, $\nu = 4/3$, $d_E = 2$, $\beta = 5/36$) gives $\kappa \simeq 1.9$. Our simulations clearly indicate that $\kappa \simeq 1.0$ which is inconsistent with the proposed result in [12]. Below we present an alternative view on the displacement pattern from that being initiated by Wilkinson [9] and used by Xu et al.. The alternative view is based upon the observation that nonwetting fluid flows in separate strands.

Fig. 9 shows two typical displacement structures that were obtained from simulations at low and high C_a on the lattice of 40×60 nodes with $M = 1$ (Table III). We observe that the nonwetting fluid (dark grey and black) generates patterns containing no closed loops. That means, following a path on nonwetting fluid will never bring us back to the starting point. The loopless structure is a direct consequence of the evidence that a tube filled with wetting fluid and surrounded on both sides by nonwetting fluid is trapped due to volume conservation of wetting fluid. Because of trapped wetting fluid, the nonwetting

8
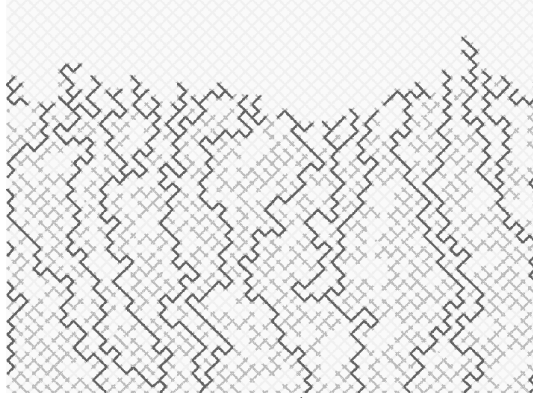
$C_a = 3.9 \times 10^{-4}, \; M = 1.0$
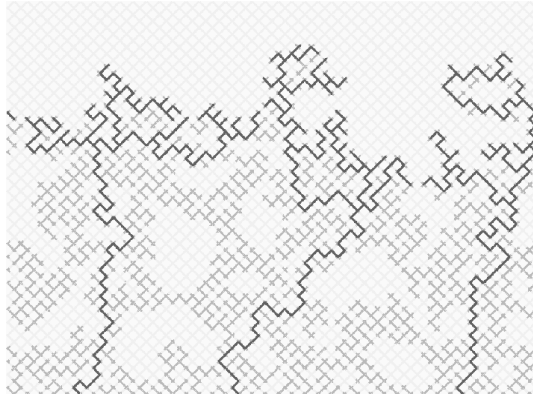
$C_a = 1.6 \times 10^{-5}, \; M = 1.0$

FIG. 9. Two displacement structures of simulations at high $C_a = 3.9 \times 10^{-4}$ (above) and low $C_a = 1.6 \times 10^{-5}$ (below) before breakthrough of nonwetting fluid. The nonwetting fluid (dark grey and black) is injected from below and wetting fluid (light grey) flows out along the top row. The lattice size was 40×60 nodes and $M = 1$ (Table III). The black tubes denote the loopless strands where nonwetting fluid flows and the dark grey tubes indicate nonwetting fluid unable to flow due to trapped regions of wetting fluid. Because of fluid trapping and subsequent volume conservation of wetting fluid, strands of different starting points along the inlet can never connect. Note the few fluid supplying strands from the inlet to the frontal region at low C_a compared to the case at high C_a.

fluid also flows in separate strands, indicated as black tubes in Fig. 9. When the nonwetting fluid percolates the system there exists only on such strand connecting the inlet to the outlet. The dark grey tubes connecting to the strands are dead ends where nonwetting fluid cannot flow because of trapped wetting fluid. We note that the evidence of trapped wetting fluid in single tubes may easily be generalized to 3D and therefore our arguments should be valid there too. Similar loopless structures as in Fig. 9, were also pointed out in [27] for site-bond IP with trapping and in [28] for a loopless IP algorithm.

From Fig. 9 we may separate the displacement patterns into two parts. One consisting of the frontal region continuously covering new tubes, and the other consisting of the more static structure behind the front. The frontal region is supplied by nonwetting fluid through a set of strands that connect the frontal region to the inlet. When the strands approach the frontal region they are more likely to split. Since we are dealing with a square lattice, a splitting strand may create either two or three new strands. As the strands proceed upwards in Fig. 9, repeatedly splits cause the frontal region to be completely covered by nonwetting strands.

On IP patterns with trapping [27] or without loops [28,29] the length l of the minimum path between two points separated an Euclidean distance R scales like $l \propto R^{D_s}$ where D_s is the fractal dimension of the shortest path. We assume that the displacement pattern of the frontal region for length less than the correlation length (in our case w_s) is statistically equal to IP patterns in [27]. Therefore, the length of the nonwetting strands in the frontal region, is proportional to Δh^{D_s} where Δh is some vertical length less than w_s. If we assume that on the average every tube in the lattice has same mobility (k_{ij}/μ_{ij}), we obtain that the fluid pressure within one strand must drop like Δh^{κ} where $\kappa = D_s$. Let us now consider the effect on the pressure when strands split. If we assume that the strands are straight $(D_s = 1)$ then following a path where strands splits would cause the pressure to drop as Δh^{κ} where $\kappa < 1$. This because the volume fluxes through the strands after a split must be less than the flux in the strand before it splits, due to volume conservation of nonwetting fluid.

The two effects $(\kappa = D_s$ and $\kappa < 1)$ predict that the pressure drop in the nonwetting phase of the frontal region, ΔP_{nw}, should scale as $\Delta P_{nw} \propto \Delta h^{\kappa}$ where $\kappa \leq D_s$. In 2D two different values for D_s have been reported: $D_s = 1.22$ [28,29] for loopless IP patterns, and $D_s = 1.14$ [27] for the single strand connecting the inlet to the outlet when nonwetting fluid percolates the system. We note that the result in [27] is essential equal to $D_{\min} = 1.13$ [25], that is the fractal dimension of the minimum path in 2D percolation where loops generally occur. Any of the above values for D_s together with the argument $\kappa \leq D_s$, are supported by our simulations finding $\kappa = 1.0 \pm 0.1$.

Note the different pattern of strands at high and low C_a in Fig. 9. At low C_a few strands are supplying the

9

frontal region with nonwetting fluid, and the strands split many times before the whole front is covered. At high C_a the horizontal distance between each strand in the static structure is much shorter, and only a few splits are required to cover the front. Moreover, we observe that at high C_a the length of individual strands in the front approaches the minimum length due to the tubes. In this limit we may treat the strands in the front as straight lines (i.e. $D_s = 1$) causing $\kappa \leq 1$. This is indeed supported by numerical results, finding that κ decreases from about 1.0 to 0.8 when increasing C_a (see Fig. 2).

Another important issue, arising at low C_a, is the effect of bursts on the capillary pressure. A burst occurs when a meniscus along the front becomes unstable and nonwetting fluid abruptly covers new tubes [22]. The strand where the burst initiates will during the burst, experiences a much higher fluid transport relative to strands far away. Describing the pressure behavior between the strand of the burst and the rest of the front is nontrivial. However, simulations show that even during bursts, we find that $\Delta P_{c\parallel}$ increases linearly with Δh.

The indication that $\kappa \simeq 1.0$, may influence the scaling behavior of w_s as function of C_a. Assuming Darcy flow where the pressure drop depends linearly on the injection rate, we conjecture that $\Delta \widehat{P}_{c\parallel} \propto C_a \Delta h^\kappa$. Here $\Delta \widehat{P}_{c\parallel}$ denotes the capillary pressure difference over a height Δh when the front is stationary. That means, $\Delta \widehat{P}_{c\parallel}$ excludes situations where nonwetting fluid rapidly invades new tubes due to local instabilities (i.e. bursts). The above conjecture is supported by simulations showing that in the low C_a regime $\Delta \widehat{P}_{c\parallel} \propto C_a \Delta h^\kappa$ where $\kappa \simeq 1.0$. Note, that $\Delta \widehat{P}_{c\parallel} \not\simeq \Delta P_{c\parallel}$ in Fig. 2, since the latter includes both stable situations and bursts.

At sufficiently low C_a the displacement may be mapped to percolation giving $\Delta \widehat{P}_{c\parallel} \propto f - f_c \propto \xi^{-1/\nu}$ [16,9,14]. Here f is the occupation probability of the bonds, f_c is the percolation threshold, and $\xi \propto w_s$ is the correlation length. By combining the above relations for $\Delta \widehat{P}_{c\parallel}$ we obtain $w_s \propto C_a^{-\alpha}$ where $\alpha = \nu/(1 + \nu\kappa)$. In 2D $\nu = 4/3$ and inserting $\kappa = 1.0$ gives $\alpha \simeq 0.57$.

In Sec. III A we found that at high C_a the nonwetting fluid invades simultaneously everywhere along the front. Hence, the front never reaches a stationary state because of rapidly succeeding local instabilities. This is supported by simulations showing a crossover in $\Delta \widehat{P}_{c\parallel}$ to a nonlinear dependency on C_a. Consequently, the above mapping to percolation might no longer be valid and we expect another type of functional behavior between w_s and C_a in the high C_a regime.

V. COMPARISON WITH EXPERIMENTS

Frette *et al.* [26] performed two phase drainage displacement experiments in a 2D porous medium with viscosity matched fluids ($M = 1$). They reported on the sta-
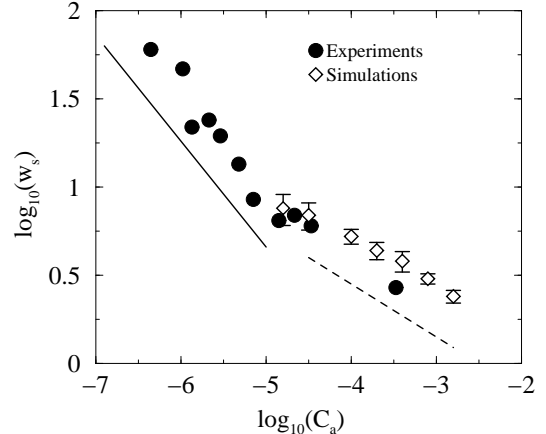

FIG. 10. $\log_{10}(w_s)$ as function of $\log_{10}(C_a)$ for experiments from [26] and simulations on the lattice of 40×60 nodes (Table III). For both experiments and simulations $M = 1$. The slope of the solid and dashed line is -0.6 and -0.3, respectively.

bilization of the front and measured the saturated front width w_s, as function of C_a. For all our simulations except those performed on the IP patterns, we have calculated w_s. In Fig. 10 we have plotted w_s as function of C_a in a logarithmic plot for the simulations in Table III, (open diamonds) together with the experimental data of Frette *et al.* (filled circles).

In [26], their best estimate of the exponent α when assuming a power law $w_s \propto C_a^{-\alpha}$ was $\alpha = 0.6 \pm 0.2$, indicated by the solid line in Fig. 10. This is consistent with the suggested value $\alpha = \nu/(1 + \nu\kappa) \simeq 0.57$ from Sec. IV. The simulations show a different behavior and they seem to fit $\alpha = 0.3 \pm 0.1$, according to the dashed line in Fig. 10. The simulations performed on the lattices of 25×35 nodes (Tables I and II) also give $\alpha \simeq 0.3$.

Even though the overlap between experimental and numerical data in Fig. 10 is poor we suggest that the different behavior of the experiments (at $C_a \lesssim 1.0 \times 10^{-5}$) and simulations (at $C_a \gtrsim 1.0 \times 10^{-5}$) might be due to an expected change in α at high C_a. According to the discussion in Sec. IV it is not clear if the percolation approach giving $\alpha = \nu/(1 + \nu\kappa)$, is valid for high C_a. The different scaling behavior observed in Fig. 10 might also be caused by the small system size of the simulations. At $C_a \simeq 1.0 \times 10^{-5}$ numerical simulations show that the front width becomes bounded by the system size, and therefore we are not able to observe a possible $\alpha = \nu/(1 + \nu\kappa)$ regime. We stress that more simulations on larger systems and at lower C_a are required in order obtain better overlap between simulations and experiments in Fig. 10. Until then, it is hard to draw any conclusions on the correct α.

As a side mark, we note that our simulations giving $\alpha \simeq 0.3$, are in agreement with numerical work in [12]. Their calculations of w_s were done for C_a between 10^{-5} and 10^{-4} coinciding with our region of simulations

in Fig. 10. According to Wilkinson [9] $\alpha = \nu/(1+t-\beta+\nu)$ and by inserting values of the exponents in 2D we obtain $\alpha \simeq 0.38$. This is also within the uncertainties of our simulation results. However, we emphasize that this might as well be a coincidence rather than an evidence, because Wilkinson's theory does not take into account that nonwetting fluid flows in strands along the front.

A somewhat different process, but very interesting result, is presented by Shaw in [30]. He measured the width of the drying front in a quasi 2D porous system and found that $w_s \propto v_f^{0.48 \pm 0.1}$. Here v_f is the average front velocity. Quite recently, this has been compared to theory in [31].

VI. CONCLUSION

We have reported on the stabilization mechanisms of the front in drainage displacement going from low to high injection rates. The stabilization process was studied by using a network model simulating the viscous and capillary pressure buildup in the fluids during the displacements. We have found that the capillary pressure difference $\Delta P_{c\parallel}$, along the front varies almost linearly with the distance Δh, in the direction of the displacement. We conclude from simulations that $\Delta P_{c\parallel} \propto \Delta h^\kappa$ where our best estimate is $\kappa = 1.0 \pm 0.1$. This result supports the arguments showing $\kappa \leq D_s$, where D_s is the fractal dimension of the loopless strands characterizing the displacement pattern. The evidence that nonwetting fluid flows in loopless strands along the front are not considered in earlier proposed theories [9–12]. Hence, we conclude that they are not compatible with drainage when nonwetting strands dominate the displacement process.

Using the evidence that $\kappa \simeq 1.0$, we conjecture that the scaling of the front width w_s as function of C_a might alters from earlier suggestions in [9,11,12]. By mapping our problem to percolation we find $w_s \propto C_a^{-\alpha}$ where $\alpha = \nu/(1+\nu\kappa)$. The result is consistent with experiments performed by Frette *et al.* [26]. Unfortunately, due to the small system sizes we are not able to confirm this scaling behavior by our simulations. We emphasize that a more stringent test on α should include simulations on larger systems and lower C_a, than presented here.

In addition to $\Delta P_{c\parallel}$ we have calculated the capillary pressure variations along the front in the direction parallel to the inlet, $\Delta P_{c\perp}$. Qualitatively, we have shown that $\Delta P_{c\perp}$ is a good indicator on whether the capillary pressures of the menisci along the front are all equal (capillary equilibrium) or fluctuating due to the viscous forces. When the capillary fluctuations are strong, we do not expect percolation to be a proper model for the displacement process.

APPENDIX A:

Below we show how to deduce $\alpha = \nu/(1+t-\beta+\nu)$ in $w_s \propto C_a^{-\alpha}$ and find the corresponding exponent $\kappa = 1+t/\nu+\beta/\nu$ in the power law $\Delta P_{c\parallel} \propto \Delta h^\kappa$ when not considering that nonwetting fluid flows through strands. The calculations are carried out in two dimension, however the extension to three dimensions is straight forward.

Let us consider a piece of the nonwetting phase of size Δh in the frontal region. We assume that $\Delta P_{c\parallel}$ vary as

$$\Delta P_{c\parallel} \propto v\Delta h^\kappa, \tag{A1}$$

where v is the average fluid velocity in the pores. Moreover, we assume that the front has reached a steady state and that the structure of the front is statistically equal to the front of an invasion percolation pattern. This assumption provides that Δh is sufficiently large for the percolation concept to apply but less than the front width w_s.

The average nonwetting pore fluid velocity v, in the the region of size Δh, is given by Darcy's law

$$v = \frac{1}{S}\frac{k}{\mu}\frac{\Delta P_{c\parallel}}{\Delta h}. \tag{A2}$$

Here S is the saturation of nonwetting phase, that is the volume fraction where nonwetting fluid can flow, and k is the permeability of the frontal region. According to percolation the frontal region is fractal, with fractal dimension $D = d - \beta/\nu$, giving

$$S \propto \frac{\Delta h^{d-\beta/\nu}}{\Delta h^d} = \Delta h^{-\beta/\nu}, \tag{A3}$$

and

$$k \propto \Delta h^{-t/\nu}. \tag{A4}$$

Here t is the conductivity exponent, β is the order parameter exponent, and ν is the correlation length exponent in percolation.

By inserting the expressions for S, k, and $\Delta P_{c\parallel}$ into Eq. (A2) we find the exponent $\kappa = 1 + t/\nu - \beta/\nu$. The exponent α follows by setting $\Delta h = w_s$ and replace $\Delta P_{c\parallel}$ in Eq. (A1) with the power law $w_s \propto \xi \propto \Delta P_{c\parallel}^{-\nu}$. Here ξ denote the correlation length in percolation.

[1] K. J. Måløy, J. Feder, and T. Jøssang, *Phys. Rev. Lett.* **55**, 2688 (1985).

[2] J.-D. Chen and D. Wilkinson, *Phys. Rev. Lett.* **55**, 1892 (1985).

[3] R. Lenormand, E. Touboul, and C. Zarcone, *J. Fluid Mech.* **189**, 165 (1988).

[4] M. Cieplak and M. O. Robbins, *Phys. Rev. Lett.* **60**, 2042 (1988).

[5] P. G. de Gennes and E. Guyon, *J. Mec. (Paris)* **17**, 403 (1978).

[6] R. Chandler, J. Koplik, K. Lerman, and J. F. Willemsen, *J. Fluid Mech.* **119**, 249 (1982).

[7] D. Wilkinson and J. F. Willemsen, *J. Phys. A* **16**, 3365 (1983).

[8] R. Lenormand and C. Zarcone, *Phys. Rev. Lett.* **54**, 2226 (1985).

[9] D. Wilkinson, *Phys. Rev. A* **34**, 1380 (1986).

[10] R. Lenormand, *Proc. R. Soc. London, Ser. A* **423**, 159 (1989).

[11] M. Blunt, M. J. King, and H. Scher, *Phys. Rev. A* **46**, 7680 (1992).

[12] B. Xu, Y. C. Yortsos, and D. Salin, *Phys. Rev. E* **57**, 739 (1998).

[13] D. Wilkinson, *Phys. Rev. A* **30**, 520 (1984).

[14] A. Birovljev, L. Furuberg, J. Feder, T. Jøssang, K. J. Måløy, and A. Aharony, *Phys. Rev. Lett.* **67**, 584 (1991).

[15] P. Meakin, A. Birovljev, V. Frette, J. Feder, T. Jøssang, K. J. Måløy, and A. Aharony, *Physica A* **191**, 227 (1992).

[16] J.-F. Gouyet, M. Rosso, and B. Sapoval, *Phys. Rev. B* **37**, 1832 (1988).

[17] S. E. Buckley and M. C. Leverett, *Trans. Am. Inst. Min. Metall. Pet. Eng.* **146**, 107 (1942).

[18] E. Aker, K. J. Måløy, A. Hansen, and G. G. Batrouni, *Transp. Porous Media* **32**, 163 (1998).

[19] E. Aker, K. J. Måløy, and A. Hansen, *Phys. Rev. E* **58**, 2217 (1998).

[20] W. B. Haines, *J. Agric. Sci.* **20**, 97 (1930).

[21] K. J. Måløy, L. Furuberg, J. Feder, and T. Jøssang, *Phys. Rev. Lett.* **68**, 2161 (1992).

[22] L. Furuberg, K. J. Måløy, and J. Feder, *Phys. Rev. E* **53**, 966 (1996).

[23] E. W. Washburn, *Phys. Rev.* **17**, 273 (1921).

[24] G. G. Batrouni and A. Hansen, *J. Stat. Phys.* **52**, 747 (1988).

[25] D. Stauffer and A. Aharony. *Introduction to Percolation Theory.* Taylor & Francis, London, 1992.

[26] O. I. Frette, K. J. Måløy, J. Schmittbuhl, and A. Hansen, *Phys. Rev. E.* **55**, 2969 (1997).

[27] M. Sahimi, M. Hashemi, and J. Ghassemzadeh, *Physica A* **260**, 231 (1998).

[28] M. Cieplak, A. Maritan, and J. R. Banavar, *Phys. Rev. Lett.* **76**, 3754 (1996).

[29] M. Porto, S. Havlin, S. Schwarzer, and A. Bunde, *Phys. Rev. Lett.* **79**, 4060 (1997).

[30] T. M. Shaw, *Phys. Rev. Lett.* **59**, 1671 (1987).

[31] I. N. Tsimpanogiannis, Y. C. Yortsos, S. Poulou, N. Kanellopoulos, and A. K. Stubos, *Phys. Rev. E* **59**, 4353 (1999).